Magnetless Nonreciprocal Metamaterial (MNM) Technology: Application to Microwave Components

Toshiro Kodera, *Senior Member, IEEE*, Dimitrios L. Sounas, *Member, IEEE*, and Christophe Caloz, *Fellow, IEEE*

***Abstract*—A magnetless nonreciprocal metamaterial (MNM), consisting of traveling-wave resonant ring particles loaded by transistor s and exhibiting the gyromagnetic properties as ferrites, without their size, weight, cost, and monolithic microwave integrated circuit incompatibility drawbacks, was recently introduced in 2011 by Kodera *et al.* This paper presents the first extensive investigation of the applicability of MNM technology to nonreciprocal microwave components. It recalls the key principle of the MNM, provides basic MNM design guidelines, explains coupling mechanism between a microstrip line and MNM rings, and demonstrates two nonreciprocal MNM components based on a microstrip-ring configuration, an isolator, and a circulator. Although these components have not been fully optimized, they already exhibit attractive performance and provide a proof-of-concept that MNM technology has a potential for microwave nonreciprocal microwave components with substantial benefits compared to their ferrite and active-circuit counterparts.**

***Index Terms*—Anisotropic and gyrotropic materials, artificial magnetism, circulators, isolators, magnetless nonreciprocal metamaterial (MNM), ring resonators.**

I. Introduction

NONRECIPROCAL microwave components—mainly isolators, circulators, gyrators, phase shifters, polarizers, switches, tunable resonators, and tunable filters [2]–[4]—are ubiquitous in modern microwave applications, including communications, radars, and sensor networks [5]–[7].

Over the past 60 years, the dominant technology for nonreciprocal microwave components has been based on *ferrites*, which are passive high-resistivity ferrimagnetic materials, such as yttrium–iron–garnet (YIG) or compounds of iron oxides, and other elements such as aluminium, cobalt, manganese, and nickel [2]–[5], [8]. However, ferrite components suffer from major drawbacks, inherent to ferrite materials, and the permanent magnet required to bias them: they are bulky, heavy, incompatible with integrated circuit technologies, expensive, sensitive to temperature detuning at lower microwave frequencies, and sometimes (ferromagnetic resonance-based devices) inapplicable at frequencies above the X-band. Recently reported self-biased ferromagnetic nanowire materials are immune to most of these drawbacks [9], but still exhibit prohibitively high loss and low power handling for commercial applications at this point.

An *active circuit* approach of nonreciprocal microwave components, where nonreciprocal effects are induced by the interconnection of transistors with a transmission line, couplers, and lumped elements in various architectures, has been explored to avoid the drawbacks of ferrite technology [10]–[14]. Unfortunately, this approach has been restricted to marginal applications, due to several issues as follows.

1) Architectures involving cascaded transistors, although providing high gain, suffer of stability issues, requiring stabilization resistors, which seriously affect the insertion loss [10].
2) The simplest—and most symmetric—circuital architectures suffer from poor performance, such as low isolation [11] or high insertion loss [13], due to inherent limited transmission efficiency, backward leakage, and all-port matching difficulty.
3) Performance improvement over these architectures, incorporating distributed couplers, leads to major increase in the size of the components, which partly defeats the initial purpose of size reduction [12], and also often breaks the symmetry of the circuit (sometimes allowing only a *quasi*-circulator [10]).
4) Nonreciprocal circuits are not materials, and are therefore inapplicable to the many components requiring distributed material effects, such as Faraday rotation, field displacement, or birefringence [2]–[5], [15]–[18].

Recently, we invented a magnetless nonreciprocal metamaterial (MNM) [1], [19]. The principle of this MNM is depicted in Fig. 1. The classical-picture current loops formed by spin electron precession in ferromagnetic materials is mimicked by electric current loops along conducting ring-pair particles loaded with a unilateral semiconductor element, typically a field-effect transistor (FET). The rotating magnetic dipole moments are produced in the midplane between the two rings of each ring-pair particle as a result of the traveling-wave propagation regime due to the FETs [1], [20]. In this work, the ring particles are arranged in a substrate plane (2-D structure) and each particle contains only one ring, a ground plane below the ring playing the role of an electric mirror from which the operation of the resulting unbalanced MNM is identical to that of a groundless balanced two-ring particle MNM. The molecular-level analogy of MNMs to ferrites distinguishes MNMs from other nonreciprocal metamaterials [35], [36], which are designed to provide some particular characteristics of ferrite-based devices, such as isolation,

Manuscript received August 28, 2012; revised December 17, 2012; accepted December 19, 2012. Date of publication January 14, 2013; date of current version March 07, 2013. This work was supported by the Natural Sciences and Engineering Research Council of Canada (NSERC) under Discovery Accelerator Supplement Grant 396116-10 and the Grant-in-Aid for Scientific Research (KAKENHI) under Grant-in-Aid 23686054.

T. Kodera is with the Department of Electrical Engineering, Yamaguchi University, Yamaguchi 7558611, Japan (e-mail: tk@yamaguchi-u.ac.jp).

D. L. Sounas and C. Caloz are with the Department of Electrical and Engineering, École Polytechnique de Montréal, Montréal, QC, Canada H2T 1J3 (e-mail: dimitrious.sounas@polymtl.ca; christophe.caloz@polymtl.ca).

Color versions of one or more of the figures in this paper are available online at http://ieeexplore.ieee.org.

Digital Object Identifier 10.1109/TMTT.2013.2238246

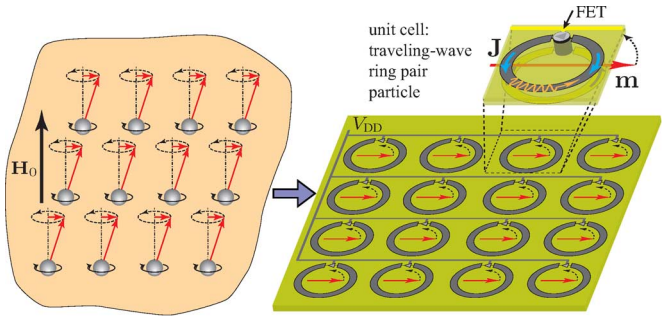

Fig. 1. Principle of the MNM (*right*), whose traveling-wave ring currents $\mathbf{J}$ induce radial rotating magnetic dipole moments $\mathbf{m}$ mimicking precession in a ferrite material (*left*).

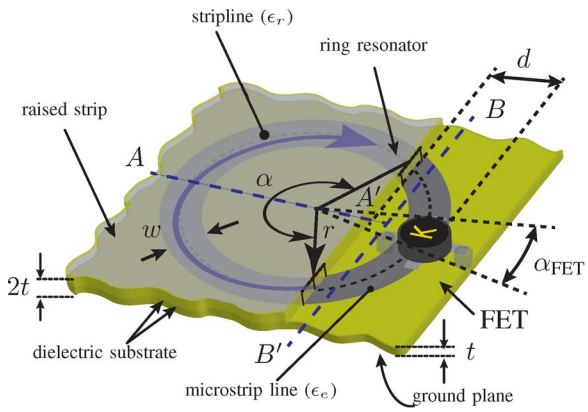

Fig. 2. Overlapping raised microstrip line and MNM ring configuration (unit cell) used in the isolator and circulator of Sections III and IV, respectively.

without exhibiting the fundamental properties of ferrites, such as Faraday rotation and field displacement.

The MNM approach to nonreciprocity might be classified between the ferrite approach (second paragraph of this section) and the active-circuit approach (third paragraph of this section). An MNM is a kind of "artificial ferrite" since it mimics the atomic activity of a ferrite material, and hence, exhibits the same fundamental properties, while it includes active elements (the FETs) like active-circuit nonreciprocal components. In contrast to active nonreciprocal circuits [10]–[14], where nonreciprocity directly stems from the unilaterality of FETs connected along transmission lines and other distributed or lumped components, an MNM is really a *material* (or a "magneto-dielectric"),[1] characterizable by a macroscopic permeability tensor [20]. Practically, it overcomes the aforementioned drawbacks of ferrites, requiring neither a ferrite nor a magnet. It is therefore lightweight, fully compatible with monolithic microwave integrated circuit (MMIC) technology, low-cost, insensitive to temperature detuning, and systematically applicable up to the upper millimeter-wave frequency range [21]. A diversity of proof-of-concept MNM structures and components have already been reported, including a Faraday polarizing surface [1], an electrically gyrotropic MNM [23], an isolator [24], a field-displacement isolator [25], a perfect electromagnetic (PEMC) metasurface [26], and a magnetless implementation [27] of the nonreciprocal ferrite leaky-wave antenna [28].

This paper presents the first extensive demonstration of some (two) MNM microwave components, with explanations of their operation principles, presentation of their basic design guidelines, and comparison to an isolated FET circuit. The components are the isolator introduced in [24] and a novel circulator. Although the number of ring-pair particles involved in the MNM structure forming these components is restricted to a few units, the corresponding MNM components still operate as ferrite components insofar as their nonreciprocity is provided by unidirectional current loops coupled to an incident wave. While the design guidelines provided are quite basic and require full-wave simulation for optimization, more accurate modeling techniques could be developed for different MNM structures in future, the first of them being already reported in [20].

This paper is organized as follows. Section II describes the planar microstrip line MNM structure considered in the paper, explains the electromagnetic coupling between the line and the MNM rings, provides a formula for the design of the rings, and characterizes the FET circuit to be used as ring loads in the components. Sections III and IV present the operation principle and results of the proposed MNM isolator and circulator, respectively, with discussions on how these components compare with their conventional counterparts. Finally, conclusions are given in Section V.

II. Structure and Design Considerations

In contrast to most previously reported MNM structures, where the electromagnetic wave is normally or obliquely incident on the ring plane(s) of the MNM (e.g., [1] and [20]), the present structure has its field propagating along the plane of the rings, as in [27]. In this case, significant phase shifts occur along the structure during the wave propagation process (spatial dispersion), and hence, the MNM structure behaves more as a mesoscopic structure than as an effective medium. However, its operation mechanism is still based on traveling-wave rotating currents along the rings, even though it may not be straightforwardly characterized by a susceptibility tensor, as in [20].

A. Microstrip MNM Structure

The MNM configuration (unit cell) used in the isolator and circulator components to be presented in Sections III and IV is depicted in Fig. 2. It is a planar structure consisting of a raised microstrip line partly overlapping the MNM rings and coupling its energy to them according to a mechanism that will be explained in Section II-B. In each unit cell, the main geometrical parameters are the average radius of the ring strip, r, the width of the ring strip, w, the angle of the strip-ring overlapping sector, α, the related ring overshoot distance, d, the angle of the FET sector, α_{FET}, and the width of the two substrates, t. Throughout this paper, all the unit cells have the same parameters.

B. Coupling Mechanism

The coupling mechanism between the raised strip and the ring in Fig. 2 may be explained by considering the electromagnetic

[1]Note that the 2-D MNM structure shown in the right of Fig. 1 may be stacked to obtain a volumetric and 3-D material [22].

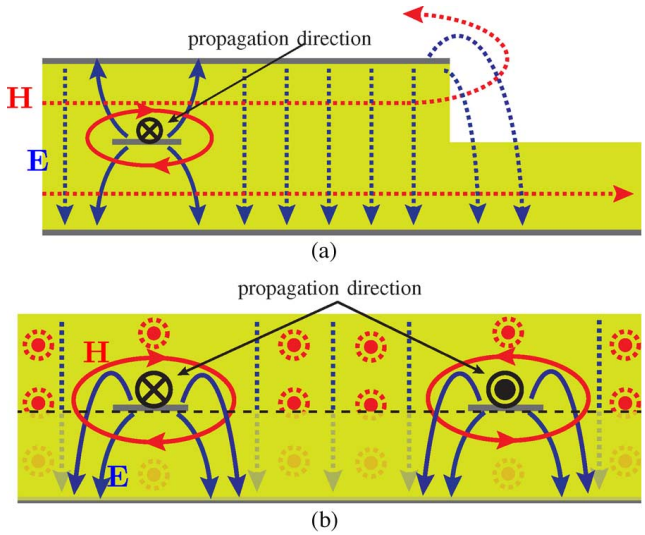

Fig. 3. Electromagnetic field lines for the isolated (without ring) raised microstrip line (dotted lines) and for the ring within the raised microstrip line structure (solid lines) in the two cross sections indicated in Fig. 2. (a) A–A'. (b) B–B'. The phase exact relation between the opposite ring strip sections depends on the overshoot distance (d) and on the electrical size of the ring (Section II-C).

field lines in the cross sections A–A' and B–B' sketched in Fig. 3 for the isolated (without ring) raised microstrip line and for the ring within the raised microstrip line structure. The comparative inspection of the field lines of these two modes will reveal the nature of the coupling and provide a qualitative idea about the amount of coupling that is expressed by the coupling coefficient [29]

$$k = \frac{\int_S \mu \mathbf{H}_1 \cdot \mathbf{H}_2 da - \int_S \epsilon \mathbf{E}_1 \cdot \mathbf{E}_2 da}{\int_S \epsilon |\mathbf{E}_1|^2 da} \tag{1}$$

where subscripts 1 and 2 refer to the raised microstrip and ring modes, respectively, μ and ϵ represent the effective permeability and permittivity, respectively, and S denotes the cross-sectional surface of interest.[2]

Fig. 3(a) sketches the fields in the A–A' cross section of Fig. 2, while Fig. 4 shows the corresponding full-wave simulated fields. It may be inferred from these fields that no coupling exists below the raised microstrip line since the electric and magnetic fields of the raised strip and ring are even and odd symmetric, respectively, with respect to the ring plane (the midplane between the raised strip and the ground) so that the coupling integral in (1) are zero.

Fig. 3(b) sketches the fields in the B–B' cross section of Fig. 2, while Fig. 5 shows the corresponding full-wave simulated fields. It may be inferred from these fields that strong electric coupling exists beyond the microstrip line since the electric field of the ring is not any more odd symmetric with respect to the ring plane, as below the raised microstrip line, so that the electric coupling integral in (1) is nonzero. On the other hand, magnetic coupling is small since close to the raised strip edge,

[2]The formula of (1) is strictly valid only for symmetric resonators [29], which does not correspond to the situation of Fig. 2. However, it still conveys the information that the coupling is proportional to the difference between the magnetic and electric coupling integrals, which is what is required for the forthcoming qualitative analysis.

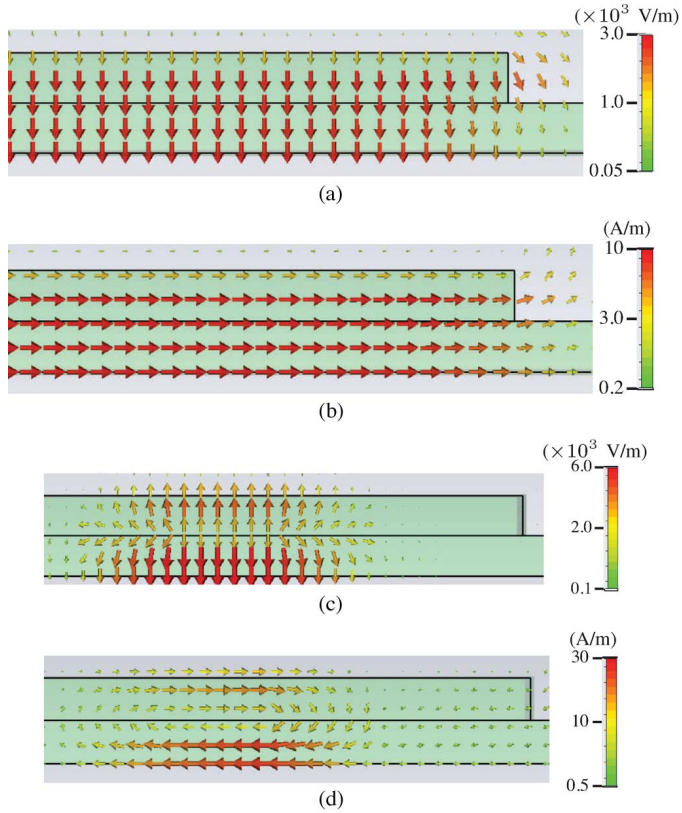

Fig. 4. Vectorial electromagnetic field (CST Microwave Studio full-wave simulation, logarithmic scale) corresponding to the A–A' cross-sectional sketch of Fig. 3(a). The design parameters corresponding to Fig. 2 are $\epsilon_r = 2.6$, $t = 0.8$ mm, $r = 5.85$ mm, $w = 2$ mm, $\alpha = 180°$ ($d = r + w/2 = 6.85$ mm), $\alpha_{\mathrm{FET}} = 30°$, a phase shift of the FET of $\phi_0 = 159°$, and a resonant frequency of $f_0 = 2.55$ GHz. (a) Electric field of the raised microstrip mode without the ring [corresponding to the dotted lines in Fig. 3(a)]. (b) Corresponding magnetic field. (c) Electric field of the ring mode within the raised microstrip structure [corresponding to the solid lines in Fig. 3(a)]. (d) Corresponding magnetic field.

where the maximum coupling is expected, the magnetic fields of the raised strip and the ring are orthogonal to each other.

Finally, Fig. 6 shows the full-wave simulated vectorial magnetic field in the plane of the substrate. Although the field magnitude is nonuniform along the circumference of the ring, due to the nonzero phase of the transistor, a magnetic rotating dipole moment, associated with the net average magnetic field, can clearly be observed, as in the MNM at the right of Fig. 1.

From the above considerations, it may be anticipated that the amount of coupling between the raised microstrip line and the ring will increase with the overshoot distance d.

C. Ring Size

The ring in Fig. 2 resonates, and therefore maximally interacts with the incoming wave, when the total phase around the ring, ϕ_{tot}, is a multiple of 2π, i.e.,

$$\phi_{\mathrm{tot}} = -[\beta_s r\alpha + \beta_{\mathrm{ms}} r(2\pi - \alpha - \alpha_{\mathrm{FET}})] + \phi_0 = 2m\pi,\ m \in \mathbb{N} \tag{2}$$

where

$$\beta_s = k_0\sqrt{\epsilon_r} = \frac{\omega_m}{c}\sqrt{\epsilon_r} \tag{3a}$$

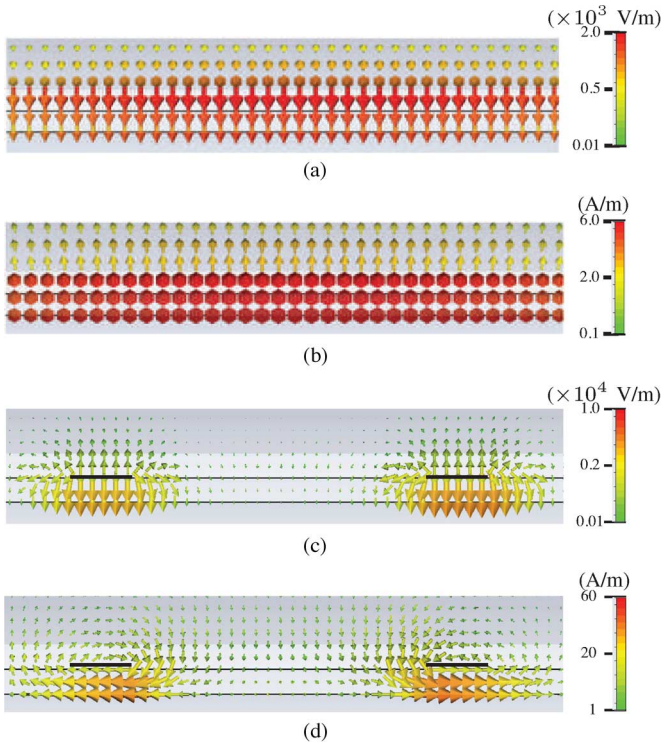

Fig. 5. Vectorial electromagnetic field (CST Microwave Studio full-wave simulation, logarithmic scale) corresponding to the B–B' cross-sectional sketch of Fig. 3(b). Same design parameters as in Fig. 4. (a) Electric field of the raised microstrip mode without the ring [corresponding to the dotted lines in Fig. 3(b)]. (b) Corresponding magnetic field. (c) Electric field of the ring mode within the raised microstrip structure [corresponding to the solid lines in Fig. 3(b)]. (d) Corresponding magnetic field.

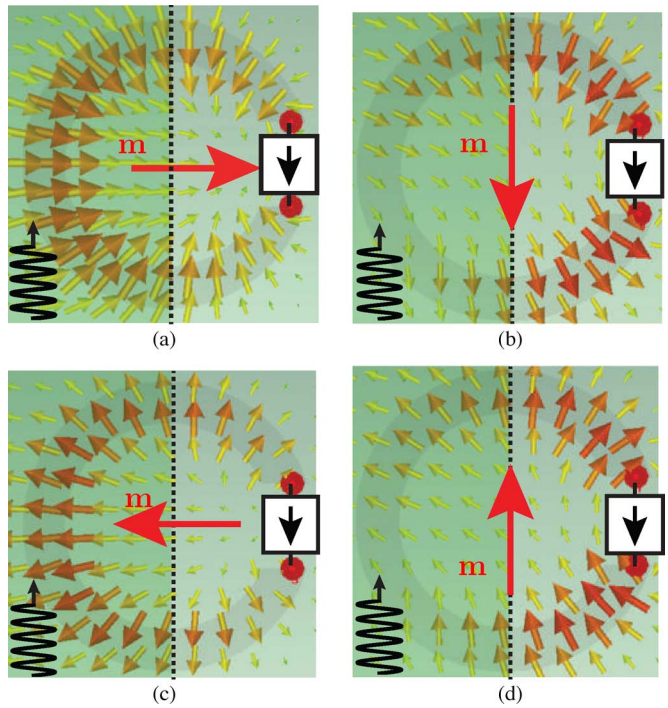

Fig. 6. Vectorial magnetic field (CST Microwave Studio full-wave simulation, linear scale) in the midplane of the lower substrate in the sketch of Fig. 2 at four instants t of the harmonic signal's period T, and corresponding rotating magnetic dipole moment $\mathbf{m}$. The shaded area at the left represents the strip line in Fig. 2. The arrowed wiggly symbol at the bottom left indicates the direction of propagation. Same design parameters as in Fig. 4. (a) $t = 0$. (b) $t = T/4$. (c) $t = T/2$. (d) $t = 3T/4$.

$$\beta_{\rm ms} = k_0\sqrt{\epsilon_e} = \frac{\omega_m}{c}\sqrt{\epsilon_e} \tag{3b}$$

are the stripline and microstrip line wavenumbers corresponding to the overlapping and nonoverlapping regions of the ring with the strip, respectively. In these relations, ϵ_r is the permittivity of the substrate and ϵ_e is the effective microstrip permittivity given by [5]

$$\epsilon_e = \frac{\epsilon_r + 1}{2} + \frac{\epsilon_r - 1}{2}\frac{1}{\sqrt{1 + 12t/w}}. \tag{4}$$

The radius of the ring particle at the mth resonance may then be found from (2) as

$$r_m = \frac{\phi_0 - 2\pi m}{\beta_{\rm s}\alpha + \beta_{\rm ms}(2\pi - \alpha - \alpha_{\rm FET})} \tag{5}$$

where the specified resonance frequency is included in $\beta_{\rm s}$ and $\beta_{\rm ms}$ via (3).

Alternatively, the mth resonance resonance frequency corresponding to a given radius r may be found by inserting (3) into (2)

$$\omega_m = \left| \frac{(\phi_0 - 2m\pi)c}{r\left[\sqrt{\varepsilon_r}\alpha + \sqrt{\varepsilon_e}(2\pi - \alpha - \alpha_{\rm FET})\right]} \right|. \tag{6}$$

Equation (6) reveals that ω_m, and consequently the operation frequency of the MNM devices, can be indefinitely increased by decreasing r, as long as the FET retains its unilateral operation and the minimum scale of the structure is larger than the fabrication tolerance.

D. Ring Loading FET Circuit

The same FET ring loading circuit (Fig. 2) will be used in the isolator (Section III) and in the circulator (Section IV). Fig. 7 shows a photograph of this circuit's prototype, with its matching and biasing networks. The FET is a Renesus NE3210S01, which has been chosen for its low-noise performance and high maximal operation frequency (20 GHz). The device is connected in a common-source configuration. It is not biased for optimal amplification, as specified by the manufacturer, but for stable unity-gain unilaterality, slightly below the transistor's saturation region. Subsequently, a bias voltage of $V_{DD} = 0.4$ V, corresponding to a drain current of $I_{DD} = 30$ mA, is applied to the drain of the FET through a narrow-width (0.2 mm) meander line with a chip inductor of 19 nH ensuring a flat gain response. Moreover, two resistors, of 68 and 100 Ω, are connected from the gate and the source to the ground, respectively, to both match the transistor to the ring microstrip line and maximize the dissipation in the attenuated direction [1], [25]. Finally, two bypass capacitors, of 1 pF and 1 μF are inserted in the bias drain line to ensure a stable broadband behavior.

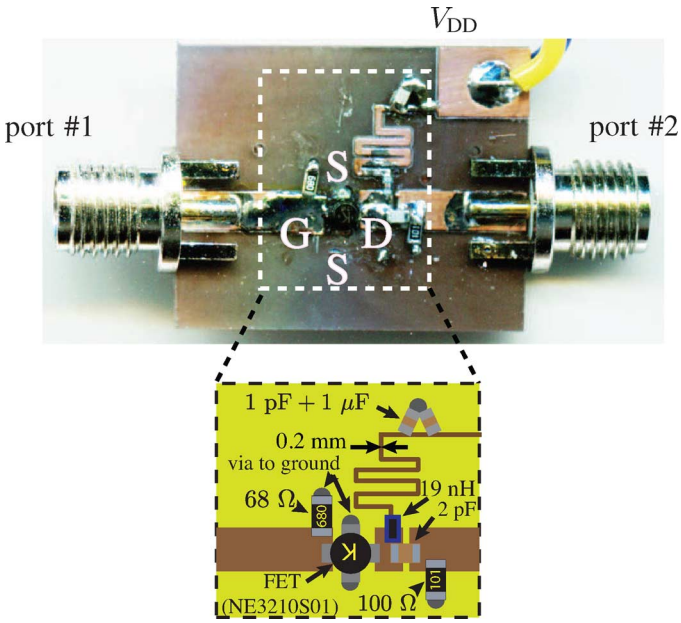

Fig. 7. Ring loading FET circuit used in the isolator (Section III) and circulator (Section IV).

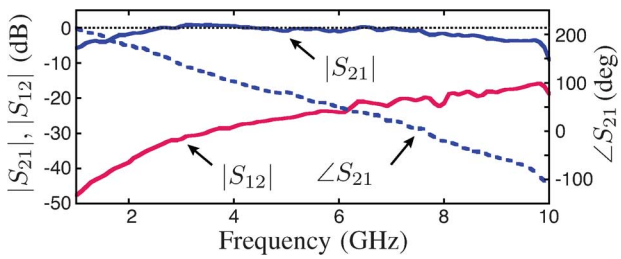

Fig. 8. Measured magnitude and phase responses of the FET circuit of Fig. 7. The effects of the connectors and connecting microstrip lines were calibrated out.

Fig. 8 shows the magnitude and phase responses of the prototype of Fig. 7. The circuit features a broad unity-gain ($|S_{21}| = 0$ dB) bandwidth, extending from about 2 to 8 GHz, across which the isolation ($|S_{21}| - |S_{12}|$) varies from about -30 to -20 dB and across which the phase ($\angle S_{21}$) varies from about 180° to $-20°$. This broad operation bandwidth will allow to accommodate both the circulator and the isolator designs, whose operation frequencies will be of 6.5 and 2.9 GHz, respectively.

III. Isolator

In ferrite technology, different types of isolators are commonly used, the most popular of them being the resonance isolators, the displacement isolators, and the Faraday isolators [2], [5]. All of these isolators can be potentially implemented in MNM technology since an MNM operates essentially as a ferrite (Section I). For instance, the proof-of-concept of a displacement isolator was reported in [25]. We present here an extensive study of an MNM isolator whose principle was first reported in [24].

A. Operation Principle

The overall configuration of the MNM isolator is shown in Fig. 9. The structure consists of a raised microstrip structure loaded by a double row of MNM rings loaded by FETs connected in opposite circular directions in the two rows.

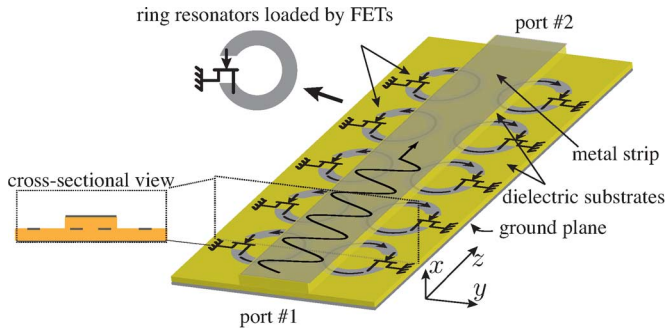

Fig. 9. MNM isolator.

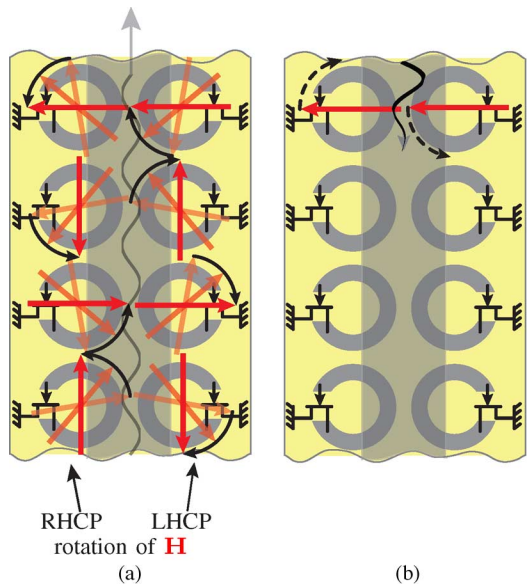

Fig. 10. Operation principle of the isolator of Fig. 9. (a) Transmission direction ($+z$). The FETs allow the propagation of the traveling-waves currents induced on the rings by the circularly polarized magnetic field of the raised microstrip line. (b) Attenuation direction ($-z$). The FETs prevent the propagation of these currents, and hence, absorb the energy of the wave.

The operation principle of the isolator may be easily understood from Section II-B and with the help of Fig. 10. The wave coming from the raised microstrip line couples to the MNM rings according to the coupling mechanism explained in Section II-B. Wave currents are subsequently induced along the rings in the same direction (below the microstrip) as the current along the microstrip line. When the wave is launched in the positive z-direction, corresponding to the case of Fig. 10(a), the current wave coupled from the microstrip line to the rings (Section II-B) flows in the directions allowed by the FETs at both sides of the raised strip. Consequently, the FET-loaded rings being essentially reactive in the passing direction, little energy is dissipated along the structure, and the wave is essentially transmitted across it. In contrast, when the wave is launched in the negative z-direction, corresponding to the case of Fig. 10(b), the current waves coupled to the rings are prevented from flowing because their direction is opposite to that allowed by the FETs. Consequently, the energy coupled to the ring has to follow a different path and essentially dissipates in the resistors used in the matching and biasing networks (Section II-D), and the wave is attenuated.

TABLE I
ISOLATOR DESIGN PARAMETERS

f_0 (GHz)	ϕ_0 (deg)	ε_r	t (mm)	w (mm)	ε_e	α (deg)	α_{FET} (deg)	r_0 (mm)
2.55	159	2.6	0.8	2.0	2.13	180	30	5.85

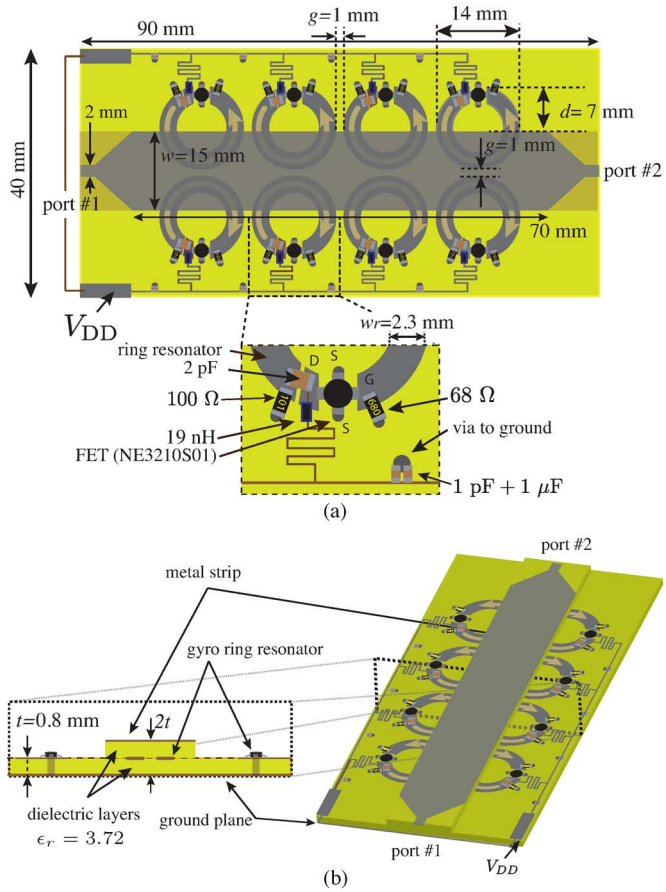

Fig. 11. Experimental prototype of the isolator with biasing network and geometrical and electrical parameters. (a) Top view. (b) Perspective and cross-sectional views.

Note that this operation principle is different from that of the double-slab ferrite resonance waveguide isolator, which is based on the interaction between circularly polarized magnetic fields at two symmetric planes of the waveguide with antisymmetrically biased ferrite slabs placed at these locations [2], [5]. The fact that it does not require any circularly polarized field is an advantage of the proposed isolator since it may then be implemented in simple transmission line (transverse electromagnetic) structures.[3]

B. Full-Wave and Experimental Results

The isolator to be demonstrated in this section is a 2.55-GHz isolator based on the $m = 0$ ring resonance for which using

[3]In [24], the interaction between the microstrip line and the MNM rings was attributed to the circularly (in fact, elliptically) polarized magnetic field of the raised microstrip line without the rings at its edges. However, the authors have later realized that this effect, although really present, is *not* the fundamental cause of the interaction. A proof of this statement was obtained by full-wave simulating the stripline counterpart of the isolator. In this case, the stripline being homogeneous, and therefore, transverse electromagnetic, the magnetic field is purely transverse and does not exhibit any rotation in the absence of the rings; nevertheless, isolation was still observed.

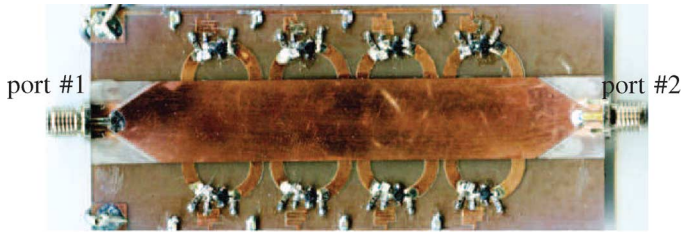

Fig. 12. Fabricated MNM isolator corresponding to Fig. 11.

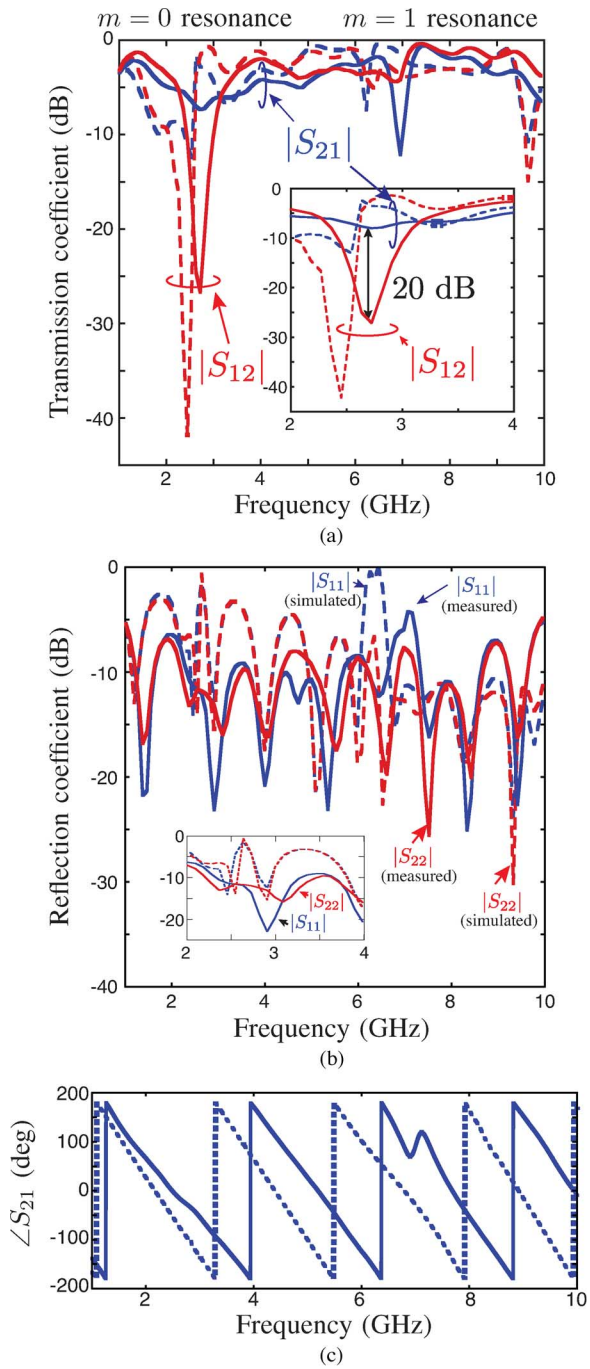

Fig. 13. Full-wave simulated (CST Microwave Studio, dotted curves) and measured (solid curves) scattering parameters for the isolator. (a) Transmission. (b) Reflection. (c) Phase, where the solid line is the measurement and the dotted line is the simulated results.

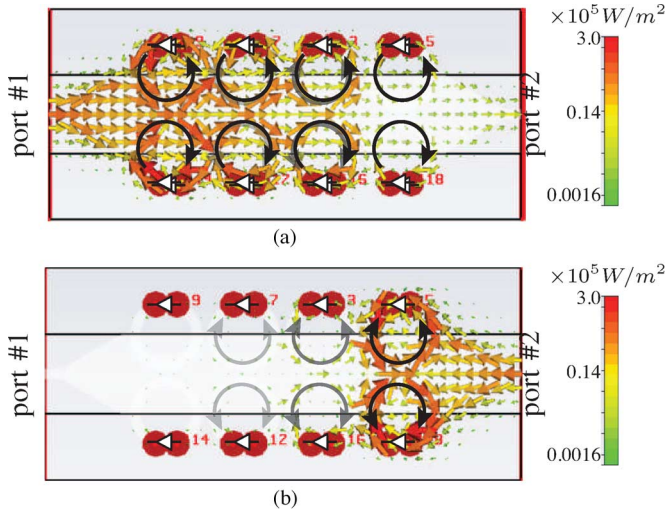

Fig. 14. Full-wave simulated Poynting vector (log scale) at the full-wave frequency of maximal isolation (2.46 GHz) in the plane of the top conductor. (a) Port 1 excitation. (b) Port 2 excitation.

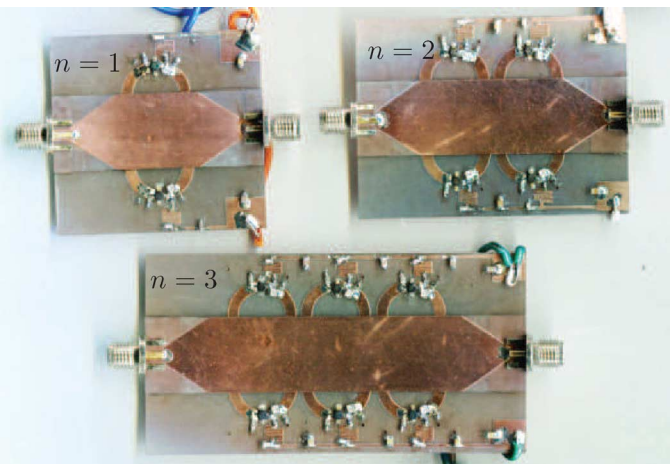

Fig. 15. Fabricated MNM isolator with one, two, and three rows of ring pairs.

the parameters of Table I and the FET phase response of Fig. 8, (5) yields a ring radius of $r_0 = 5.85$ mm. Fig. 11 shows the exact isolator structure of the experimental prototype, while a photograph of the corresponding fabricated prototype is shown in Fig. 12.

Fig. 13 plots the full-wave simulated and measured scattering parameters for the isolator of Fig. 12. In the analytical and numerical calculations, the FETs are modeled using the measured scattering parameters of Fig. 7. The experimental $m = 0$ resonance frequency, of 2.7 GHz, is quite close to the design frequency of 2.55 GHz. The close proximity of the resonance of the entire structure to the resonance of the isolated ring leads to the conclusion that the coupling between the rings plays a minor role on the operation frequency of the device. The isolation, defined as $|S_{21}|-|S_{12}|$, is 20.0 dB, the insertion loss is 6.8 dB, and return losses are $S_{11} = -23$ dB and $S_{22} = -18$ dB. The 20-dB isolation bandwidth is 50 MHz. Another isolation frequency is observed at 6.2 GHz. This is the $m = 1$ ring resonance frequency. It is smaller then $m = 0$ because the component has been optimized for the latter. This isolator prototype has not been extensively optimized, and should therefore be considered mostly as a proof-of-concept.

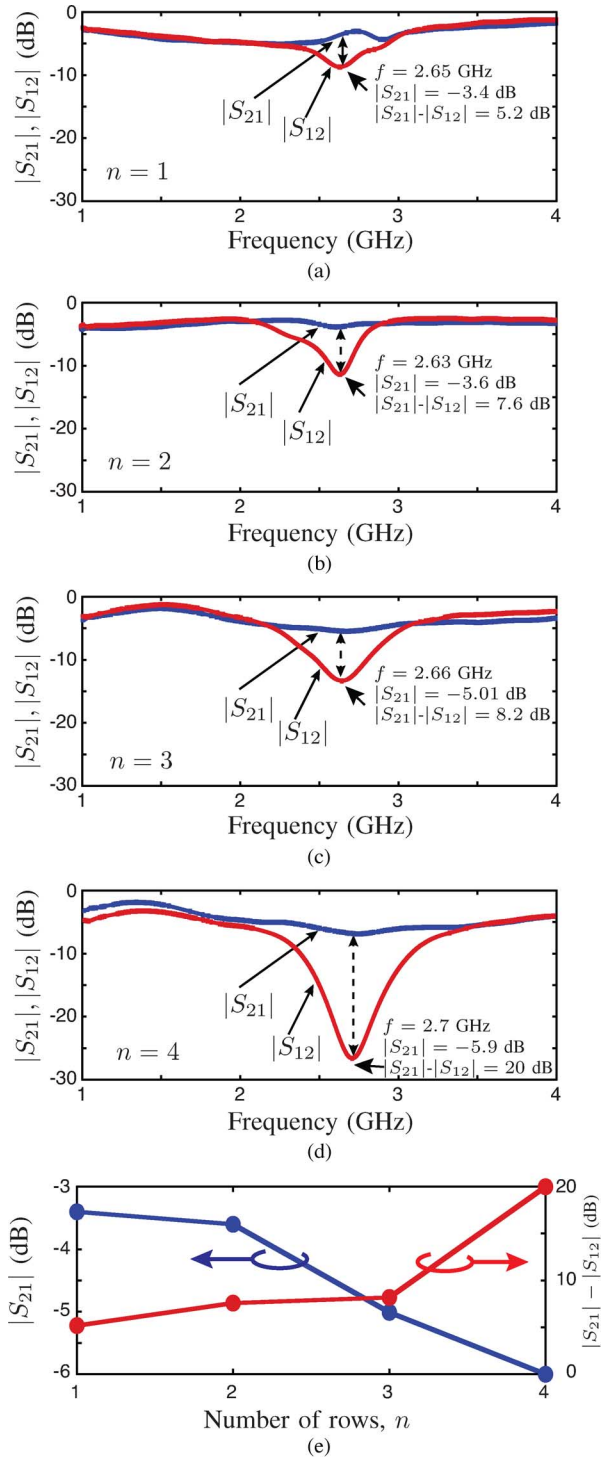

Fig. 16. Measured scattering parameters for isolators with: (a) $n = 1$, (b) $n = 2$, and (c) $n = 3$ (Fig. 15), and (d) $n = 4$ (Fig. 12). (e) S_{21} and $|S_{21}| - |S_{12}|$ versus n at the maximum isolation frequency in (a)–(d).

Fig. 14 shows the full-wave simulated power flow (Poynting vector) in the plane of the raised strip for excitations at the two ports. The reactive and absorption coupling effects in the transmission and attenuation directions, respectively, are clearly observable in this figure.

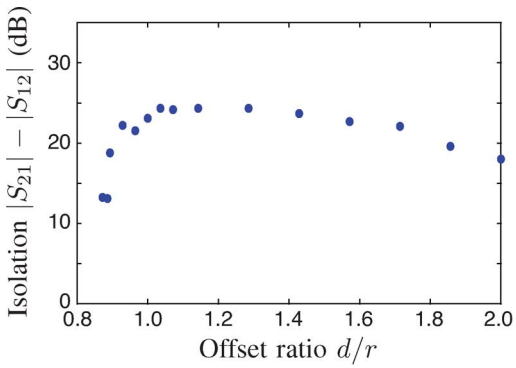

Fig. 17. Full-wave simulated isolation versus the overshoot distance of the ring, d (Fig. 2), normalized to the ring's radius.

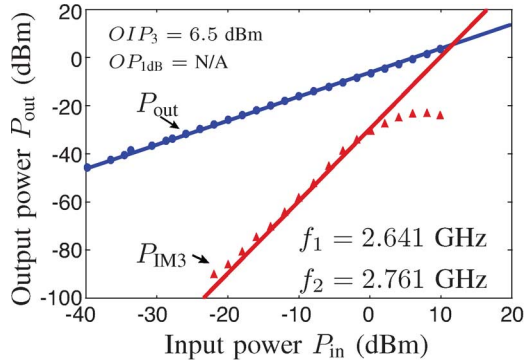

Fig. 18. Measured nonlinearity and intermodulation of the isolator of Fig. 12.

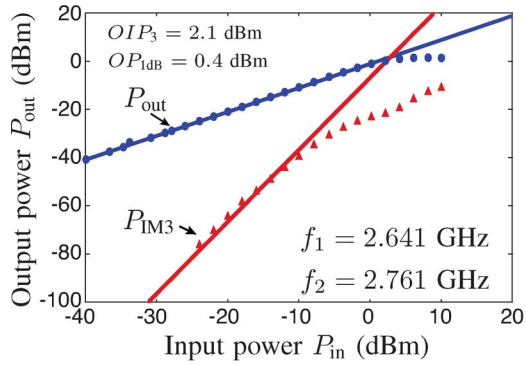

Fig. 19. Measured nonlinearity and intermodulation of the isolated FET circuit of Fig. 7.

The simulated power-flow for excitation at port #2 in Fig. 14 may suggest a prior possibility to reduce the number of ring rows (transverse pairs) since most of the power is absorbed by the first row from port #2. If the level of isolation were maintained, reducing the number of rows would be desirable since it would both reduce the size and the insertion loss of the component. In order to investigate the effect of the number of rows on the performance, isolators with one, two, and three rows were fabricated, as shown in Fig. 15 for the same parameters as in Fig. 11. Fig. 16 shows the corresponding measured responses. The results indicate that the single-row isolator exhibits an isolation 15 dB lower then the four-row isolator, with an insertion loss increase of about 2.5 dB. Fig. 16(e) shows the tradeoff between the isolation and insertion loss.

Fig. 17 presents the isolation ($|S_{21}| - |S_{12}|$) versus the overshoot distance of the ring, d in Fig. 2. Note that since d strongly affects the coupling between the rings and the raised strip, Fig. 17 essentially shows the effect of the coupling on the structure performance. As d is increased from a situation where most of the ring is beneath the microstrip line ($d < r$), the isolation increases quickly until half of the ring overshoots the microstrip line ($d = r$), where it reaches a maximum, and then slowly decreases as the ratio of overshooting further increases ($d > R$). This dependence on d indicates that, as could have been expected, the amount of isolation is proportional to the coupling from the microstrip line to the rings. Indeed, the coupling is close to zero when the ring is mostly beneath the microstrip and becomes maximal for $d = r$, where the the microtrip-ring nonoverlapping area is maximal, as shown in Section II-B. When $d > r$, the coupling naturally decreases due to increased distance from the microstrip line.

Finally, Fig. 18 shows the measured nonlinearity and intermodulation of the isolator. No power saturation is observed up to 10-dBm input power and the third-order intermodulation output level is of 6.5 dBm. The maximal power of 10 dBm was imposed by the available generator. According to measurements (not presented here), the power handling of the isolator is not affected by the number of rows. In contrast, the nonlinear characteristics of the devices are mostly determined by the first row since the power decreases from row to row due to dissipation.

A glance at Fig. 8 suggests that a simple FET on a transmission line (Fig. 7) represents a better isolator than the MNM isolator since it features a smaller size, a broader bandwidth, and lower power consumption with a comparable (or larger) isolation. This is certainly true if this simple FET circuit meets the linearity and power-handling specifications for the isolator. When this is not the case, the FET-circuit approach would require a power-splitting approach with multiple FETs (power division → array of 2 or more FETs → power combination), where each transistor would drive only a fraction of the total power. This would suppress the size, bandwidth, and power consumption benefits of the resulting component since quarter-wavelength type splitters would have to be introduced into the circuit [5], [33]. Moreover, this would involve matching issues in the case of a large number of FET channels. In this case, the MNM isolator may offer benefits: 1) for a comparable size; 2) comparable power consumption; and 3) potentially broader[4] bandwidth, superior linearity, and power-handling properties could be obtained. To provide a quantitative notion of this statement, Fig. 19 plots the measured nonlinearity and intermodulation of the simple FET circuit (Fig. 7) and Table II compares the isolation performance of this circuit with that of the MNM isolator. In contrast to the MNM isolator, which is perfectly linear up to 10-dBm input power (Fig. 18), the FET circuit has a 1-dB output compression point of only 0.4 dBm (Fig. 19). Moreover, it exhibits a 4.4-dB smaller output third-order intermodulation point. The superior linearity performance of the MNM isolator

[4]A broader bandwidth could be obtained by using two concentric rings of different diameters in constituent particle. The response of the particle would then be the superposition of the responses of the two concentric rings. If the rings were designed so that their resonances were adequately close, the superposition could provide a broader bandwidth response from the combined particle.

TABLE II
COMPARISON OF THE SIMPLE FET CIRCUIT (FIG. 7) AND THE MNM ISOLATOR (FIG. 12) PERFORMANCE AT $f_1 = 2.7$ GHz (BIASING $V_{DD} = 0.4$ V)

	OIP_3 (dBm)	OP_{1dB} (dBm)	Isolation (dB)	P_{DC} (mW)
FET circuit	2.1	0.4	24.7	13.0
MNM isolator	6.5	N/A	20.0	112

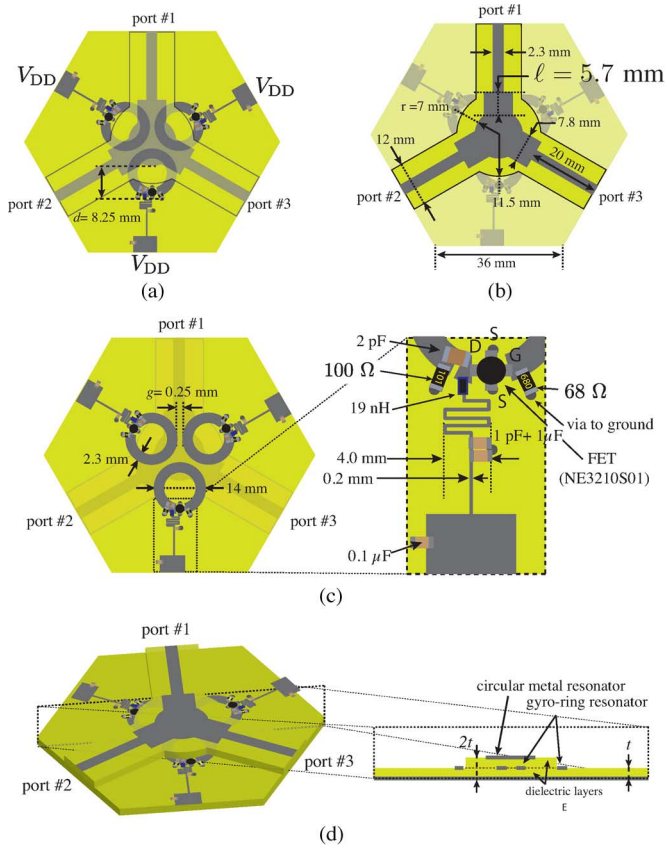

Fig. 20. Proposed MNM circulator. (a) Top view of the whole structure. (b) Dimensions for the top layer. (c) Dimensions for the bottom layer (*left*) and detailed matching and bias network (*right*). (d) Perspective (*left*) view and cross-sectional (*right*) view. All the material parameters are the same as in Fig. 3.

is mainly due to the electromagnetic power splitting between the two ring rows of the MNM structure. While the aforementioned power-splitter approach could be used in the simple FET circuit, splitting and separation becomes difficult and inefficient for more than two or three FETs. In contrast, the MNM isolator could feature several layers of rings, easily implementable in MMIC technology, where the power would be automatically split between the different rings at each point by electromagnetic coupling.

IV. CIRCULATOR

The circulator is one of the most essential microwave nonreciprocal components [2], [3], [5]. As pointed out in Section I, the active-circuit based circulators suffer from a major issue [10]–[14]: they are either perfectly symmetric (i.e., exhibiting a symmetric circulator scattering matrix response [5]), but inefficient [10] or relatively efficient by imperfectly symmetric (i.e., without circulation between all ports) [13]. We present here an MNM-based circulator, which avoid this issue along with the main drawbacks of ferrite isolators (Section I).

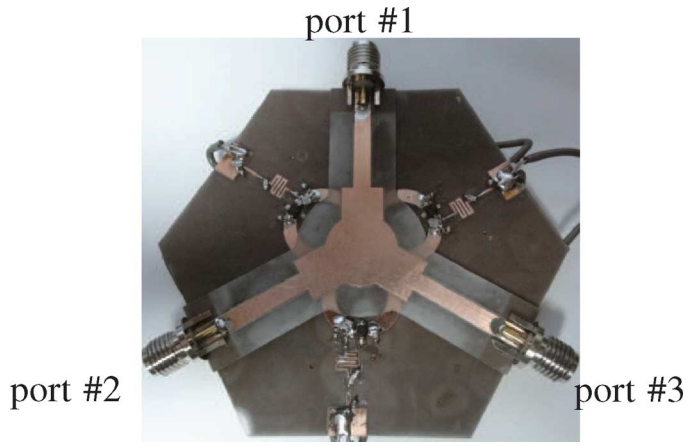

Fig. 21. Fabricated MNM circulator corresponding to Fig. 20.

TABLE III
CIRCULATOR DESIGN PARAMETERS

f_0 (GHz)	ϕ_0 (deg)	ε_r	t (mm)	w (mm)	ε_e	α (deg)	α_{FET} (deg)	r_0 (mm)
6.5	37.5	2.6	0.8	2.0	2.13	110	30	5.85

A. Operation Principle

Fig. 20 shows the proposed MNM circulator along with design parameters, while Fig. 21 shows the corresponding fabricated prototype.[5] Although the component includes only three MNM rings, its operation principle is related to that of a conventional ferrite circulator [2], [5]. The coupling between the MNM rings through the central cavity, via the same coupling mechanism as in the MNM isolator (Section II-B), generates two azimuthally counter-propagating modes. The unilateral nature of propagation along the rings splits off these modes in frequency, and the superposition of these split modes at their median frequency provides the circulating effect of the circulator. The authors have developed an electromagnetic modeling for this MNM circulator. However, this modeling is too involved to be integrated in this paper and will therefore be presented elsewhere.

B. Full-Wave and Experimental Results

The circulator to be demonstrated in this section is based on the $m = 1$ ring resonance with a resonance frequency $f_0 = 6.5$ GHz, for which, using the parameters of Table III and the FET phase response of Fig. 8, (5) yields a ring radius of $r_0 = 5.85$ mm (same radius as for the isolator).

The exact structure of the experimental circulator prototype, along with its matching and biasing network and geometrical

[5]Note that, while the top substrate of the raised microstrip line was restricted to the area of the elevated strip in the case of the isolator (Fig. 11), the top substrate here was chosen to extend beyond the width of the strips for easier conventional microstrip characterization [conventional microstrip lines on a substrate of thickness $2t$, as shown in Fig. 20(d)] of the lines.

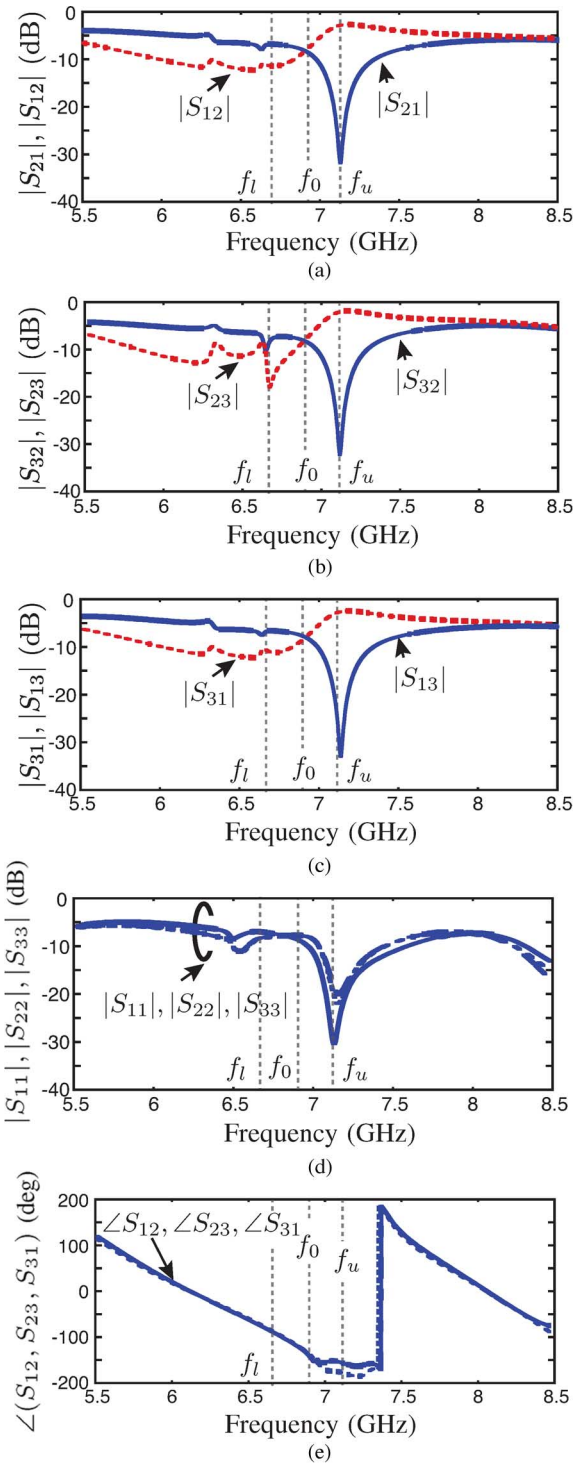

Fig. 22. Full-wave simulated (CST Microwave Studio) scattering parameters for the circulator of Fig. 20.

and electrical parameters, was shown in Fig. 20. As in the isolator case (Section III), the FETs are modeled using the measured scattering parameters of Fig. 7 in the analytical and numerical calculations.

The central circular patch cavity of this circulator is quite different from that of ferrite circulators due to the strong inter-coupling effects of the rings. Therefore, no attempt was made to

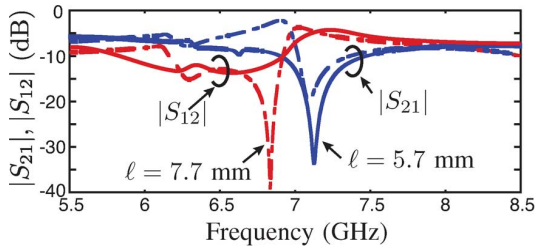

Fig. 23. Full-wave simulated (CST Microwave Studio) scattering parameters for $\ell = 5.7$ mm and $\ell = 7.7$ mm in Fig. 20(b).

design a resonant cavity as in ferrite circulators. Rather, the three-port microstrip lines where designed as simply interconnected at the center of the structure by a circular patch junction via rectangular matching section. The dimensions of the circular and rectangular patches were tuned by full-wave simulations, and further, in the experiment, by using copper tape.

Fig. 22 plots the full-wave simulated scattering parameters of the MNM circulator. The MNM circulator, just as a conventional ferrite circulator [2], exhibits two counter-directed circulation frequencies located around an effective cavity resonance (without circulation), occurring here at $f_0' = 6.9$ GHz, which is remarkably close to the design frequency ($f_0 = 6.5$ GHz), given the approximations associated with (5) for this structure. Although a strong clockwise circulation resonance is observed at $f_u = 7.13$ GHz with an isolation of 30 dB, the counter-clockwise circulation resonance observed at $f_l = 6.6$ GHz is weak. As seen in Fig. 22(d), the low isolation at f_l is accompanied by high insertion loss, which suggests that the weak response at f_l results from inadequate matching at this frequency.

Fig. 23 plots the full-wave simulated scattering parameters between port #1 and #2 for a different matching condition with $\ell = 5.7$ mm and $\ell = 7.7$ mm in Fig. 20(b). This result clearly indicates the asymmetric circulation at f_l and f_u are due to mismatch.

Fig. 24 plots the experimental scattering parameters of the MNM circulator. The center, clockwise, and counterclockwise frequencies, $f_0' = 7.1$ GHz, $f_u' = 7.45$ GHz, and $f_l = 6.8$ GHz, are shifted by approximately 0.2 GHz toward higher values with respect to numerical results, most likely due to deviations from the substrate permittivity of the simulated one. Similarly to numerical simulations, at $f_u' = 7.45$ GHz, a large isolation of 30 dB is obtained, while the isolation at $f_l' = 6.8$ GHz is weaker with a value around 15 dB. Furthermore, as in numerical simulations, the insertion loss at f_l' is much higher than at f_u'.

The measured insertion loss of 5 dB with 20-dB isolation bandwidth of 150 MHz represent a performance that is inferior to that of state-of-the-art commercial ferrite circulators [34]. One possible reason for the relatively high insertion loss may be the resistive impedance matching of the FET isolator. In the current device configuration, a low-loss conjugate matching network using capacitors and inductors or transmission line sections is not applicable due to space limitations. However, in MMIC implementations, this issue may be avoided by FET internal matching.

Fig. 25 shows the full-wave simulated power flow (Poynting vector) along the circulator structure for excitations at the three

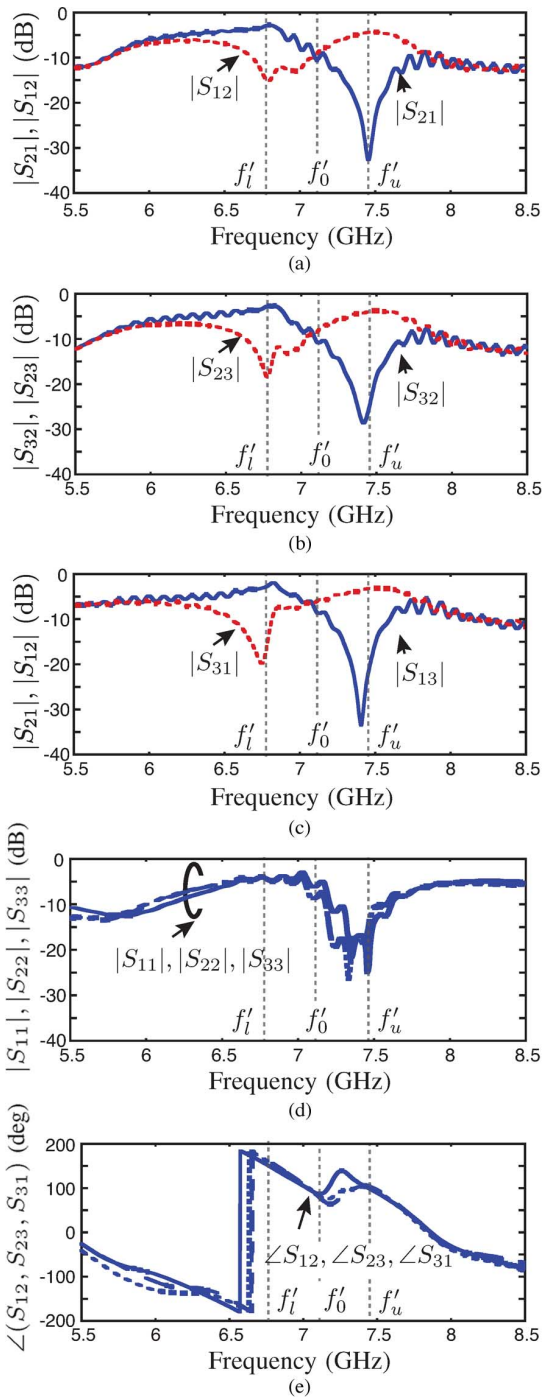

Fig. 24. Measured scattering parameters for the circulator of Fig. 21.

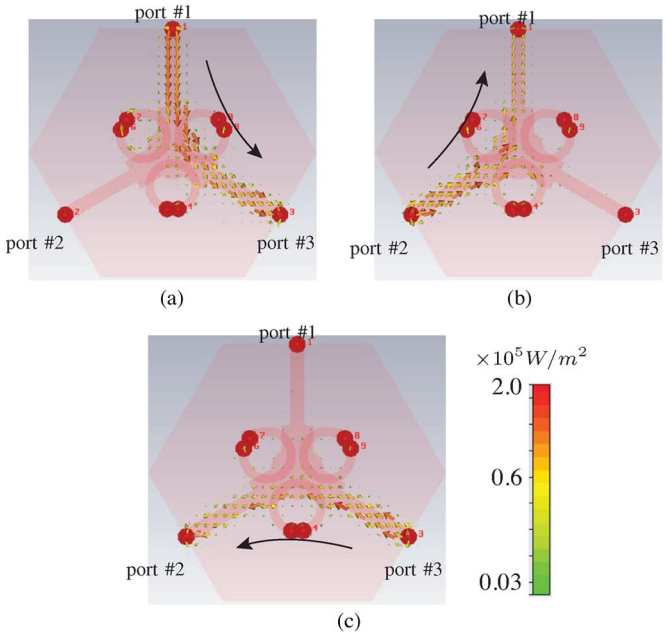

Fig. 25. Full-wave simulated Poynting vector (log scale) at the full-wave maximum isolation frequency ($f_u = 7.13$ GHz) in the plane of the top conductor. (a) Excitation at port 1. (b) Excitation at port 2. (c) Excitation at port 3.

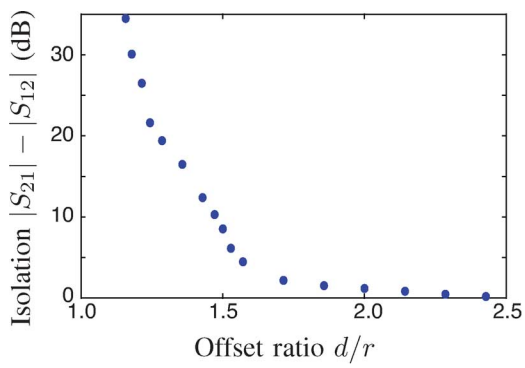

Fig. 26. Full-wave simulated circulator isolation versus the overshoot distance of the ring, d (Fig. 20), normalized to the ring's radius.

TABLE IV
PERFORMANCE COMPARISON OF SIMPLE FET ISOLATOR AND THE CIRCULATOR AT $f'_u = 7.45$ GHz AND $V_{DD} = 0.42$ V

	OIP_3 (dBm)	OP_{1dB} (dBm)	Isolation (dB)	P_{DC} (mW)
FET circuit	−1.6	−5.5	23.0	12.6
MNM circulator	−0.8	−3.4	31.5 (average)	46.2

ports at the upper circulation frequency. The perfect circulation symmetry, following from the geometrical symmetry of the structure, is clearly apparent.

Fig. 26 presents the isolation $|S_{21}| - |S_{12}|$ versus the overshoot distance of the ring, d in Fig. 20. Similar to the isolator case, Fig. 26 essentially shows the effect of coupling between the rings on the circulator performance. As d is increased from a situation where the rings are almost touching each other beneath the circular patch, the isolation monotonically decreases to zero. This behavior may also have been expected from the coupling mechanism explained in Section II-B since already more than half of the ring is overshooting the strip patch region ($d > r$) at the initial position.

Finally, Figs. 27 and 28 and Table IV compare the linearity performance of the MNM circulator and isolated FET circuit at the upper circulation frequency. As expected and as in the isolator case, the linearity is superior in the MNM case, due to electromagnetic power splitting. In the circulator, the 1-dB power compression and the OIP_3 level exceed to the corresponding of the isolated FET circuit by 2.1 and 1 dB, respectively. The

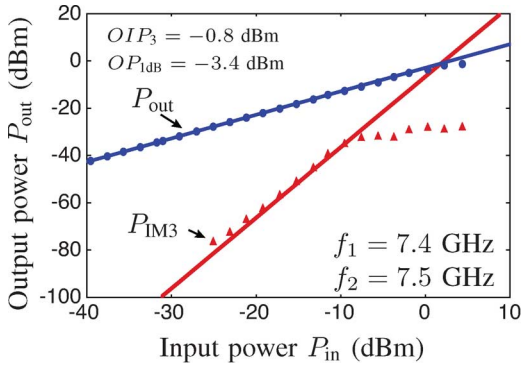

Fig. 27. Measured nonlinearity and intermodulation of the MNM circulator of Fig. 21 at for the transmission from ports 2 to 1 at the frequency of $f_u' = 7.45$ GHz.

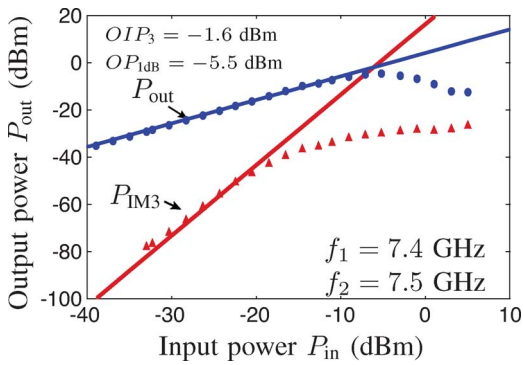

Fig. 28. Measured nonlinearity and intermodulation of the isolated FET circuit of Fig. 7 used in the circulator of Fig. 21 at the frequency of $f_u' = 7.45$ GHz. The biasing conditions are $V_{DD} = 0.42$ V and $I_D = 0.03$ A.

power-handling requirements of the device will determine the type of FET (e.g., GaAs or GaN FET) to be chosen.

V. Conclusion

This paper has presented the first extensive investigation of the applicability of MNM technology to microwave nonreciprocal components. It has provided basic MNM design guidelines, explained the coupling mechanism between a microstrip line and MNM rings, and demonstrated two nonreciprocal MNM components based on a microstrip-ring configuration, an isolator, and a circulator.

Although these components have not been fully optimized, they already exhibit attractive performance and provide a proof-of-concept that MNM technology has a potential for microwave nonreciprocal microwave components with substantial benefits compared to their ferrite and active-circuit counterparts. These components suggest that MNM technology has a significant potential for low-cost, small-size, and high-frequency nonreciprocal microwave devices. MNM technology may be easily deployed in MMICs.

Acknowledgment

The authors would like to acknowledge the CST Corporation, Darmstadt, Germany, for their generous donation of CST software licenses.

References

[1] T. Kodera, D. L. Sounas, and C. Caloz, "Artificial Faraday rotation using a ring metamaterial structure without static magnetic field," *Appl. Phys. Lett.*, vol. 99, pp. 031114:1–031114:3, Jul. 2011.
[2] B. Lax and K. J. Button, *Microwave Ferrites and Ferrimagnetics*. New York: McGraw-Hill, 1962.
[3] A. Goldman, *Modern Ferrite Technology*, 2nd ed. Berlin, Germany: Springer, 2010.
[4] J. Adam, L. Davis, G. Dionne, E. Schloemann, and S. Stizer, "Ferrite devices and materials," *IEEE Trans. Microw. Theory Techn.*, vol. 50, no. 3, pp. 721–737, Mar. 2002.
[5] D. M. Pozar, *Microwave Engineering*, 4th ed. New York: Wiley, 2011.
[6] A. F. Molish, *Wireless Communications*, 2nd ed. Hoboken, NJ: Wiley, 2011.
[7] E. Lutz, M. Werner, and A. Jahn, *Satellite Systems for Personal and Broadband Communications*. Berlin, Germany: Springer, 2000.
[8] A. G. Gurevich and G. A. Melkov, *Magnetization Oscillations and Waves*. Boca Raton, FL: CRC, 1996.
[9] L.-P. Carignan, A. Yelon, D. Ménard, and C. Caloz, "Ferromagnetic nanowire metamaterials: Theory and applications," *IEEE Trans. Microw. Theory Techn.*, vol. 59, no. 10, pp. 2568–2586, Oct. 2011.
[10] S. Tanaka, N. Shimomura, and K. Ohtake, "Active circulators—The realization of circulators using transistors," *Proc. IEEE*, vol. 53, no. 3, pp. 260–267, Mar. 1965.
[11] Y. Ayasli, "Field effect transistor circulators," *IEEE Trans. Magn.*, vol. 25, no. 5, pp. 3242–3247, Sep. 1989.
[12] I. Bahl, "The design of a 6-port active circulator," in *IEEE MTT-S Int. Microw. Symp. Dig.*, May 1988, pp. 1011–1012.
[13] M. Smith, "GaAs monolithic implementation of active circulators," in *IEEE MTT-S Int. Microw. Symp. Dig.*, May 1988, pp. 1015–1016.
[14] G. Carchon and B. Nanwelaers, "Power and noise limitations of active circulators," *IEEE Trans. Microw. Theory Techn.*, vol. 48, no. 2, pp. 316–319, Feb. 2000.
[15] R. I. Hunter, D. A. Robertson, P. Goy, and G. M. Smith, "Design of high-performance millimeter wave and sub-millimeter wave quasi-optical isolators and circulators," *IEEE Trans. Microw. Theory Techn.*, vol. 55, no. 5, pp. 890–898, May 2007.
[16] A. Shahvarpour, T. Kodera, A. Parsa, and C. Caloz, "Arbitrary electromagnetic conductor boundaries using faraday rotation in a grounded ferrite slab," *IEEE Trans. Microw. Theory Techn.*, vol. 58, no. 11, pp. 2781–2793, Nov. 2010.
[17] A. Parsa, A. Shahvarpour, and C. Caloz, "Double-band tunable magnetic conductor realized by a grounded ferrite slab covered with metal strip grating," *IEEE Microw. Wireless Compon. Lett.*, vol. 21, no. 5, pp. 231–233, May 2011.
[18] A. Parsa, T. Kodera, and C. Caloz, "Ferrite based non-reciprocal radome, generalized scattering matrix analysis and experimental demonstration," *IEEE Trans. Antennas Propag.*, vol. 59, no. 3, pp. 810–817, Mar. 2011.
[19] T. Kodera, C. Caloz, and D. Sounas, "Artificial magnetic material, artificial magnetic device, artificial magnetic material reflecting wall and artificial magnetic material transparent wall," Int. Patent Appl. PCT/CA2011/001422, Dec. 22, 2011.
[20] D. L. Sounas, T. Kodera, and C. Caloz, "Electromagnetic modeling of a magnetless nonreciprocal gyrotropic metasurface," *IEEE Trans. Antennas Propag.*, vol. 61, no. 1, pp. 221–231, Jan. 2013.
[21] *MMIC Design*, I. D. Robertson, Ed. London, U.K.: IEE Press, 1995.
[22] D. L. Sounas, T. Kodera, and C. Caloz, "Network modeling of multilayer magnet-less non-reciprocal gyrotropic metamaterials," in *IEEE AP-S Int. Symp.*, Jul. 2012, pp. 1–2.
[23] T. Kodera, D. L. Sounas, and C. Caloz, "Faraday rotation by artificial electric gyrotropy in a transparent slot-ring metamaterial structure," in *IEEE AP-S Int. Symp.*, Jul. 2012, pp. 1–2.
[24] T. Kodera, D. L. Sounas, and C. Caloz, "Isolator utilizing articial magnetic gyrotropy," in *IEEE MTT-S Int. Microw. Symp. Dig.*, Jun. 2012, pp. 1–3.
[25] T. Kodera, D. L. Sounas, H. V. Nguyen, H. Razavipour, and C. Caloz, "Field displacement in a traveling-wave ring resonator meta-structure," in *30th URSI Gen. Assemb. Sci. Symp.*, Aug. 2012, pp. 1–4.
[26] T. Kodera, D. L. Sounas, and C. Caloz, "PEMC metamaterial surface whose gyrotropy is provided by travelling-wave ring resonators," in *IEEE AP-S Int. Symp.*, Oct. 2011, pp. 1–4.
[27] T. Kodera, D. L. Sounas, and C. Caloz, "Non-reciprocal magnet-less CRLH leaky-wave antenna based on a ring metamaterial structure," *IEEE Antennas Wireless Propag. Lett.*, vol. 10, no. 1, pp. 1551–1554, Jan. 2012.

[28] T. Kodera and C. Caloz, "Uniform ferrite-loaded open waveguide structure with CRLH response and its application to a novel backfire-to-endfire leaky-wave antenna," *IEEE Trans. Microw. Theory Techn.*, vol. 57, no. 4, pp. 784–795, Apr. 2009.
[29] I. Awai and Y. Zhang, "Overlap integral calculation of resonator coupling," in *12th Int. Antenna Technol. Appl. Electromagn. and URSI Symp./CNC Conf.*, Jul. 2006, pp. 589–592.
[30] J. D. Jackson, *Classical Electrodynamics*, 4th ed. New York: Wiley, 1998.
[31] M. Makimoto and S. Yamashita, *Microwave Resonators and Filters for Wireless Communication: Theory, Design and Application*. Berlin, Germany: Springer, 2001.
[32] T. Kodera and C. Caloz, "Low-profile leaky-wave electric monopole loop antenna using the $\beta = 0$ regime of a ferrite-loaded open waveguide," *IEEE Trans. Antennas Propag.*, vol. 58, no. 10, pp. 3165–3174, Oct. 2010.
[33] T. H. Lee, *The Design of CMOS Radio-Frequency Integrated Circuits*, 2nd ed. Cambridge, U.K.: Cambridge Univ. Press, 2003.
[34] J. Helszajn, *The Stripline Circulators: Theory and Practice*. Hoboken, NJ: Wiley, 2008.
[35] B. Popa and S. Cummer, "Nonreciprocal active metamaterials," *Phys. Rev. B, Condens. Matter*, vol. 85, pp. 205101:1–205101:6, May 2012.
[36] M. Tsutsumi and T. Ueda, "Nonreciprocal left-handed microstrip lines using ferrite substrate," in *IEEE MTT-S Int. Microw. Symp. Dig.*, Jun. 2004, vol. 1, pp. 249–252.

Toshiro Kodera (M'01–SM'12) received the B.E., M.E., and Dr. Eng. from the Kyoto Institute of Technology, Kyoto Japan, in 1996, 1998, and 2001, respectively.

He developed some numerical program and devices using ferrite media. In 2001, he joined the Faculty of Engineering, Osaka Institute of Technology, as a Lecturer. In 2005, he joined Wave Engineering Laboratories, ATR International, Kyoto, Japan, as an Visiting Researcher, and in 2006, he became a Researcher. While with ATR International, he was engaged in research and development of GaAs MMICs for 802.15.3c Gb/s wireless local area network (WLAN) systems and microwave power amplifiers. In 2008, he joined the Department of Electrical Engineering, École Polytechnique of Montréal, where he developed some microwave/millimeter-wave radiative structures by magnetic material as a Research Associate. In 2010, he joined the Department of Electrical Engineering, Yamaguchi University, Yamaguchi, Japan, where he is currently an Associate Professor. His current research is focused on microwave devices utilizing artificial magnetic gyrotropy including active structures, passive structures, and nanostructures.

Dr. Kodera was the recipient of several awards including the 2010 Michiyuki Uenohara Memorial Award, the 2010 MTT-S Japan/Kansai Chapter Young Engineer Award, and the 2009 European Microwave Conference (EuMC) Young Engineers Prize as a coauthor.

Dimitrios L. Sounas (M'11) was born in Thessaloniki, Greece, in September 1981. He received the Diploma and Ph.D. degrees in electrical and computer engineering from the Aristotle University of Thessaloniki (AUTH), Thessaloniki, Greece, in 2004 and 2009, respectively.

From August 2010 to October 2012, he was a Post-Doctoral Fellow with the Electromagnetic Theory and Applications Research Group, École Polytechnique of Montréal. In November 2012, he joined the Metamaterials and Plasmonics Research Group, The University of Texas at Austin, as a Post-Doctoral Fellow. His research interests include analytical and numerical techniques in electromagnetics, metamaterials, and graphene-based structures.

Christophe Caloz (S'00–A'00–M'03–SM'06–F'10) received the Diplôme d'Ingénieur en Électricité and Ph.D. degree from the École Polytechnique Fédérale de Lausanne (EPFL), Lausanne, Switzerland, in 1995 and 2000, respectively.

From 2001 to 2004, he was a Postdoctoral Research Engineer with the Microwave Electronics Laboratory, University of California at Los Angeles (UCLA). In June 2004, he joined the École Polytechnique of Montréal, where he is currently a Full Professor, a member of the Poly-Grames Microwave Research Center, and the Holder of a Canada Research Chair (CRC). He has authored or coauthored over 450 technical conference, letter, and journal papers and 12 books and book chapters. He holds several patents. His works have generated about 10 000 citations. His research interests include all fields of theoretical, computational, and technological electromagnetics engineering with a strong emphasis on emergent and multidisciplinary topics, particularly those including nanoelectromagnetics.

Dr. Caloz is a member of the IEEE Microwave Theory and Techniques Society (IEEE MTT-S) Technical Committees MTT-15 (Microwave Field Theory) and MTT-25 (RF Nanotechnology). He is a speaker of the MTT-15 Speaker Bureau, the chair of Commission D (Electronics and Photonics), Canadian Union de Radio Science Internationale (URSI), and an IEEE MTT-S representative with the IEEE Nanotechnology Council (NTC). He was the recipient of several awards, including the University of California at Los Angeles (UCLA) Chancellor's Award for post-doctoral research (2004), the IEEE MTT-S Outstanding Young Engineer Award (2007), and many Best Paper Awards with his students.